Applied Catalysis B: Environmental 125 (2012) 288–293

Contents lists available at SciVerse ScienceDirect

Applied Catalysis B: Environmental

journal homepage: www.elsevier.com/locate/apcatb

Low temperature-synthesis of $BiVO_4$ nanorods using polyethylene glycol as a soft template and the visible-light-activity for copper acetylacetonate decomposition

Sho-ichi Eda, Musashi Fujishima, Hiroaki Tada*

Department of Applied Chemistry, School of Science and Engineering, Kinki University, 3-4-1, Kowakae, Higashi-Osaka, Osaka 577-8502, Japan

ARTICLE INFO

Article history:
Received 20 February 2012
Received in revised form 21 May 2012
Accepted 27 May 2012
Available online 4 June 2012

Keywords:
Bismuth vanadate
Nanoparticles
Low-temperature synthesis
Visible light photocatalysis

ABSTRACT

Monoclinic sheelite $BiVO_4$ nanorods (*ms*-$BiVO_4$ NRs) have been synthesized from an aqueous solution of $Bi(NO_3)_3$ and NH_4VO_3 at 370 K containing polyethylene glycol (PEG), while micron-sized $BiVO_4$ crystals (*ms*-$BiVO_4$ MCs) are formed without PEG. The UV–vis absorption spectra of the PEG solutions of NH_4VO_3 suggested the formation of a complex consisting of VO_3^- ion and PEG. In this synthetic route, PEG can suppress the reactivity of VO_3^- ions by the stabilization to further act as a soft template for the formation of *ms*-$BiVO_4$ NRs. The as-grown *ms*-$BiVO_4$ NRs exhibit a high level of photocatalytic activity for the degradation of $Cu(acac)_2$ without sacrificial agents under illumination of visible-light ($\lambda > 430$ nm). The local symmetry of VO_4 tetrahedron affecting the light absorption intensity in addition to the large surface area and high crystallinity have been suggested to be a crucial factor to achieve the high visible-light-activity of *ms*-$BiVO_4$.

1. Introduction

TiO_2 photocatalyst is the most promising "eco-catalyst" for purifying polluted water and air, and recovering precious metals [1]. However, TiO_2 cannot effectively utilize sunlight as an energy source due to the wide band gap above 3 eV. While a great deal of effort has currently being devoted to endowing TiO_2 with visible-light-activity [2,3], various narrow gap semiconductors have newly been developed. Among them, $BiVO_4$ has recently attracted much interest as a visible-light-photocatalyst [4]. Usually, sacrificial agents such as Ag^+ ions and H_2O_2 are necessary for $BiVO_4$ to show high visible-light-activities for the reactions including the O_2 generation from water [5,6], and the degradation of organic pollutants [7,8]. This is probably because the conduction band (CB) edge of $BiVO_4$ (ca. 0 V vs. standard hydrogen electrode (SHE)) [5,6] is too low for the electron transfer to H^+ and O_2, which are electron acceptors in the ordinal photocatalytic reactions, to occur efficiently. We have recently reported that $BiVO_4$ exhibits a high level of visible-light-activity for the $Cu(acac)_2$ degradation and the following Cu recovery from the solution without external sacrificial agents [9]. There are two points in this reaction: one is that $Cu(acac)_2$ is strongly adsorbed on *ms*-$BiVO_4$ usually showing low adsorptivity for organic compounds [10–12], and the other is that Cu^{2+} ions generated through the oxidation of the acetylacetonate-ligands by the valence band (VB) holes act as a good mediator for the electron transfer from the CB to O_2.

$BiVO_4$ particles can be prepared by various methods including the solid-state reaction [5,6,13], ultrasonic spray pyrolysis [14], the solution combustion [15], the co-precipitation [16], the hydrothermal synthesis [17–19], and the aqueous solution synthesis [20]. The reaction temperatures (T_r) in these processes are on the order of T_r (solid-state reaction) > 973 K, T_r (ultrasonic spray pyrolysis) = 973 K, T_r (solution combustion) > 773 K, T_r (co-precipitation) > 473 K, T_r (hydrothermal) > 433 K, T_r (aqueous solution) ≈ 298 K. In general, the key to increase the activity of semiconductor photocatalysts is the compatibility of the high crystallinity and the large surface area [21]. While the high temperature processes enable to synthesize $BiVO_4$ with high crystallinity, the specific surface areas of the particles prepared by the solid-state reaction are low: ~0.3 $m^2\,g^{-1}$ (solid-state reaction), 1.6 $m^2\,g^{-1}$ (solution combustion), and 1.5 $m^2\,g^{-1}$ (co-precipitation). In spite of the high-temperature process, ultrasonic spray pyrolysis yields the particles with a fairly large surface area of 3.2 $m^2\,g^{-1}$. An aqueous solution process has been developed, where monoclinic and tetragonal $BiVO_4$ crystals can be synthesized selectively by controlling the Bi/V ratio in the solution [20]. However, the specific surface area remains 2.4 $m^2\,g^{-1}$ even by the room-temperature method. Interestingly, *ms*-$BiVO_4$ nanoparticles with surface areas more than 10 $m^2\,g^{-1}$ [17,18] and various morphologies [19] have recently been prepared by hydrothermal routes. However, the hydrothermal synthesis needs high pressure and reaction temperatures above 473 K. For energy saving, the development of low-temperature wet processes for producing $BiVO_4$ nanoparticles is highly expected. On the other hand, the nanometer-sized crystalline formation from alcoholic solution (NAC-FAS) method involving the reflux of a H_2O-alcohol mixed solution of metal

* Corresponding author. Tel.: +81 6 6721 2332; fax: +81 6 6727 2024.
E-mail address: h-tada@apch.kindai.ac.jp (H. Tada).

0926-3373/$ – see front matter © 2012 Elsevier B.V. All rights reserved.
http://dx.doi.org/10.1016/j.apcatb.2012.05.038

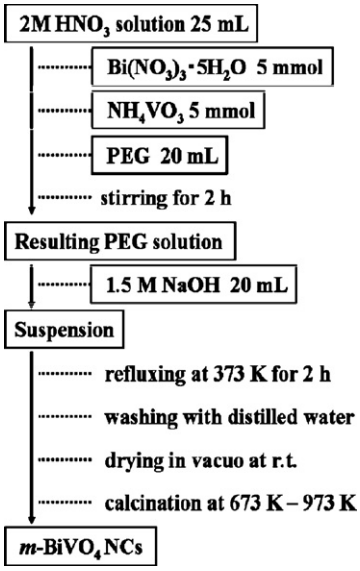

Fig. 1. Flowchart for synthesizing m-$BiVO_4$ NCs.

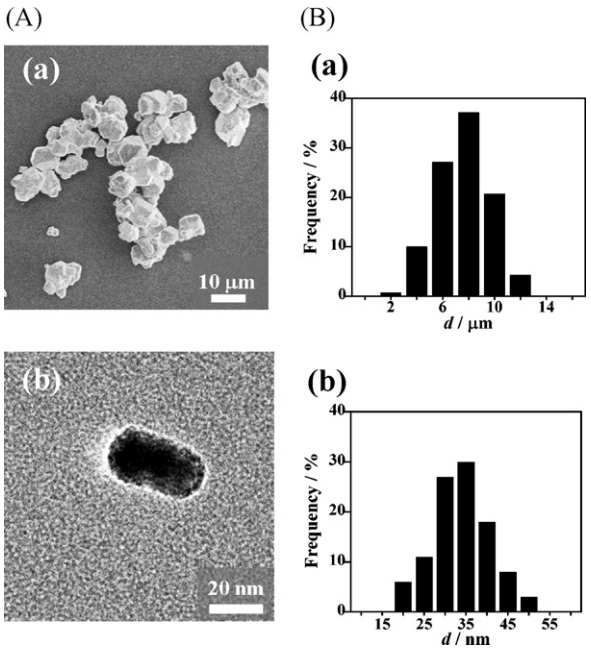

Fig. 2. SEM and TEM images (A), and particle size distribution (B) for the samples prepared without (a) and with (b) PEG.

complexes or metal salts is a useful technique for preparing various metal oxide nanoparticles including ZnO [22], TiO_2 [21], and Co^{2+}-doped TiO_2 [23].

Here we report the synthesis of *ms*-$BiVO_4$ nanorods (NRs) with a specific surface area of 8.8 $m^2\ g^{-1}$ by a nanometer-sized crystalline formation from polyethylene glycol solution (NAC-PEG) method, where the alcohol in the NAC-FAS method is replaced by PEG. The visible-light-activity of the *ms*-$BiVO_4$ NRs for the $Cu(acac)_2$ degradation was examined as a function of postheating temperature in order to clarify the factors affecting the reactivity.

2. Experimental methods

2.1. Catalyst preparation

The procedures for synthesizing *ms*-$BiVO_4$ NRs are shown in Fig. 1. $Bi(NO_3)_3{\cdot}5H_2O$ (15 mmol), NH_4VO_3 (15 mmol), and polyethylene glycol with a molecular weight of 200 (PEG-200) were dissolved into 2 M HNO_3 solution (25 mL), and then magnetically stirred for 2 h. After adding 1.5 M NaOH (20 mL), the resulting solution was heated at 370 K for 2 h. The solids obtained were washed with distilled water, and then dried in a vacuum desiccator at room temperature. The particles were calcined at temperatures ranging from 673 to 973 K in air.

2.2. Characterization of $BiVO_4$ NRs

Powder X-Ray diffraction (XRD) measurements were performed using Rigaku RINT2500. The crystalline size (d_{XRD}) was calculated from the Scherrer formula of $d_{XRD} = K\lambda/(\beta_s \cos\theta)$, where λ is the wavelength of the X-ray radiation (0.1541 nm), K is usually taken as 0.9, and β_s is the peak width at half-maximum. Transmission electron microscopic (TEM) observation was carried out using JEOL JEM-3000F at an applied voltage of 300 kV. The specific surface area was determined by nitrogen adsorption–desorption isotherms at 77 K with a micromeritics automatic surface area and porosimetry analyzer (TriStar 3000, Shimadzu). Prior to the nitrogen adsorption, all samples were degassed at 423 K for 1 h under vacuum. Diffuse reflectance UV–vis spectra were recorded on a Hitachi U-4000 spectrometer mounted with an integrating sphere at room temperature. The reflectance (R_∞) was recorded with respect to a reference of $BaSO_4$, and the Kubelka–Munk function ($F(R_\infty)$) expressing the relative absorption coefficient was calculated by the equation of $F(R_\infty) = (1 - R_\infty)^2/2R_\infty$. Photoluminescence (PL) spectra were measured with an excitation wavelength of 400 nm at room temperature or 77 K using a JASCO FP-6000 spectrofluorometer. Raman spectra were recorded on a Raman spectrometer (JASCO FP-1000). A green laser (532 nm) was used as an excitation source.

2.3. Photocatalytic activity evaluation

After the suspension of $BiVO_4$ (200 mg) in a $Cu(acac)_2$ solution (40 μM, H_2O:CH_3CN = 99:1 (v/v) or 30–400 μM, H_2O: CH_3CN = 99:1 (v/v), 200 mL) had been stirred at 298 K in the dark, irradiation was started using a 300 W Xe lamp (HX-500, Wacom) with a cut off filter Y-45 (Asahi glass co.) in a double jacket type reaction cell (31 mm in diameter and 175 mm in length). The reaction temperature was kept at 298 K by circulating thermostated water through the outer jacket around the cell. The light intensity integrated from 420 to 485 nm ($I_{420-485}$) was measured to be 3.6 mW cm^{-2}. The $Cu(acac)_2$ concentration was determined by UV–vis spectroscopy (UV-1800, Shimadzu).

3. Results and discussion

As-grown solids showed bright yellow, turning orange after postheating at temperatures above 873 K. The additive effect of PEG on the size and shape of the particles was examined. Fig. 2 shows the SEM and TEM images (left, A) and particle size distribution (right, B) for the samples prepared without (a) and with (b) PEG. In the absence of PEG, micron-sized particles are formed with a large size distribution. The PEG addition greatly decreases the particle size to yield nanoparticles with a mean particle size of 31.3 nm, resulting in fairly uniform particle formation (standard deviation, σ = 6.7 nm). Many rod-shaped nanoparticles were observed as shown in Fig. 2A(b), while some large aggregates coexisted.

To identify the solids obtained, power XRD measurements were carried out. Fig. 3A shows the XRD patterns for the samples postheated at various temperatures (T_c). In the XRD pattern for the as-grown nanoparticles, sharp peaks are present at 2θ = 18.7, 29.0,

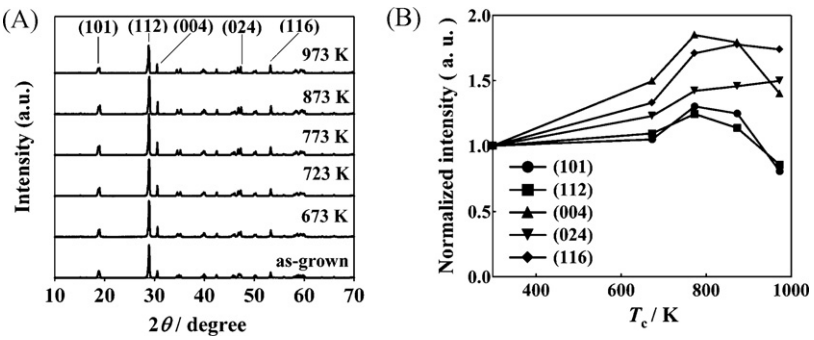

Fig. 3. (A) XRD patterns for the samples heated at varying temperatures (T_c). (B) Relative diffraction peak intensities as a function of T_c with respect to those for the as-grown sample.

Table 1
Physical properties of *ms*-BiVO4 MCs and NRs.

	d_{XRD} (nm)	S_{BET} ($m^2\ g^{-1}$)	E_g (eV)	k ($10^{-2}\ min^{-1}$)
As-grown	20.5	8.8	2.41	14.4
673 K	21.6	3.62	2.41	15.5
773 K	37.6	1.3	2.44	5.7
873 K	27.7	1.2	2.40	6.1
973 K	33.8	0.6	2.39	8.4
$BiVO_4$ MCs	–	0.2	2.43	2.0

and 31.0°, which are assignable to the diffraction from the (1 1 0), (1 1 2), and (2 0 0) crystal planes of *ms*-$BiVO_4$, respectively (JCPDS No. 01-074-4893). $BiVO_4$ has three crystal forms of zircon structure with tetragonal, sheelite structures with monoclinic and tetragonal, and *ms*-$BiVO_4$ has been shown to exhibit a higher photocatalytic activity as compared to those of the other crystal structures [6]. The relative diffraction intensity of the (1 1 2) plane is significantly larger than that in the randomly oriented sample. The diffraction peaks become sharp as the T_c increases up to 773 K, whereas the peak intensity decreases at $T_c \geq 873$ K. Clear splitting of the peaks near $2\theta \sim 35°$ at $T_c \geq 673$ K indicates the increase in the crystallinity by the postheating [24]. The micron-sized sample prepared without PEG was also confirmed to be *ms*-$BiVO_4$ (*ms*-$BiVO_4$ MCs). Table 1 summarizes the crystalline size calculated from the Scherrer equation (d_{XRD}), and the specific surface area determined by the Brunauer–Emmet–Teller method (S_{BET}) of the samples with varying T_c. For the as-grown sample, a fairly large S_{BET} of 8.8 $m^2\ g^{-1}$ is obtained. As a result of the increase in T_c, the S_{BET} monotonically decreases due to sintering, while the d_{XRD} increases up to T_c = 773 K, decreasing at $T_c \geq 873$ K. Fig. 3B shows the relative diffraction peak intensities as a function of T_c with respect to those for the as-grown sample. Every diffraction peak intensifies with increasing T_c at $T_c \leq 773$ K due to the increase in crystallinity. Heating at $T_c \geq 873$ K causes the decrease in the peak intensity, which would result from the defect-induced crystal distortion [4,6]. Evidently, this low-temperature method using PEG as a particle size control agent yields *ms*-$BiVO_4$ NRs in a single phase. The yield of $BiVO_4$ in this process was ca. 86%.

In the semiconductor photocatalysis, the mobility of the photogenerated charge carriers is an important factor for the photocatalytic activity, depending on the crystallinity as well as impurity [25]. Also, Kudo et al. reported that the local structure as well as crystallinity affects the photocatalytic activity for the O_2 evolution from an $AgNO_3$ aqueous solution [26]. Raman spectra were measured to gain the information about the bulk and local structures of *ms*-$BiVO_4$ NRs. Fig. 4A shows Raman spectra for *ms*-$BiVO_4$ NRs with varying T_c. In the spectrum for the as-grown sample, only a signal due to the symmetric V—O stretching mode (B_1) is observed at 827 cm^{-1}. At T_c = 673 K, new signals appear at 367 and 324 cm^{-1}, which can be assigned to the symmetric bending mode (B_2) and the antisymmetric bending mode of VO_4^- anion (B_3), respectively [27]. Further, in the spectra for the samples with $T_c \geq 773$ K, weak signal due to the antisymmetric V—O stretching mode (B_4) is present at 718 cm^{-1}. As a result of the increase in T_c, the intensity of B_1 significantly increases at $T_c \leq 773$ K, and then decreases at $T_c \geq 873$ K. This trend parallel to that in the XRD data reflects the bulk crystallinity of *ms*-$BiVO_4$. On the other hand, the emergence of the forbidden B_4 band at $T_c \geq 773$ K suggests that the local symmetry of *ms*-$BiVO_4$ is reduced by the postheating.

Further, the information about the electron trap levels can be obtained from photoluminescence (PL) measurements. Fig. 4B shows PL spectra for *ms*-$BiVO_4$ NRs with varying T_c. In the PL spectra for the as-grown sample, a broad signal around 655 nm (E_1) and a sharper signal at 602 nm (E_2) are observed. In the spectrum for the sample with T_c = 973 K, only the E_2 signal is present, while the E_1 disappears. The decrease in the E_1 signal intensity with increasing T_c suggests that the E_1 band arises from the emission from the surface oxygen vacancy [28]. On the other hand, the E_2 signal intensifies at T_c = 973 K, while it remains regardless of T_c. From the XRD data, the E_2 signal is tentatively assigned to the emission from the defect levels in the bulk. Uniquely, at T_c = 773 K, a broad signal (E_3) appears around 550 nm. This finding indicates the formation of new shallow trap sites further causing the distortion of the local structure (Fig. 4A). Consequently, the crystallinity of *ms*-$BiVO_4$ increases with increasing T_c at $T_c \leq 773$ K, whereas a local distortion in the structure is induced by the defects in the bulk at T_c = 773 K, and the crystallinity is lowered at $T_c \geq 873$ K.

The optical property of semiconductors is directly related to their photocatalytic activity. Fig. 5A shows UV–vis absorption spectra for the samples with varying T_c: $F(R_\infty)$ expresses the Kubelka–Munk function. In each spectrum, the absorption band due to the transition from the valence band maximum (VBM) to the conduction band minimum (CBM) is present at the wavelength below ca. 550 nm. Recent density functional theory calculations for the *ms*-$BiVO_4$ crystal have shown that the VBM and CBM mainly consist of the nonbonding O2p and the nonbonding V3d states, and the interband transition is allowed along the polarization direction of $E//a$ and $E//c$ [29]. The direct band gap (E_g) was determined from the $[F(R_\infty)h\nu]^2$ vs. $(h\nu - E_g)$ plot, where $h\nu$ is the photon energy [30]. The numerical E_g values are also shown in Table 1. The E_g is almost independent of T_c (2.42 ± 0.03 eV), and the value lies within the reported values for *ms*-$BiVO_4$ (2.4–2.5 eV) [4]. The absorption tail extends over 525 nm in the samples with $T_c \geq 873$ K, which would stem from the defects in the bulk. The absorption intensity at 470 nm ($F(R_\infty)$ at 470 nm) is also shown as a function of T_c in Fig. 5B. The absorption intensity goes through a maximum at T_c = 673 K to decrease significantly at $T_c \geq 773$ K. This decrease in the absorption intensity of the allowed transition for the samples at $T_c \geq 773$ K is ascribable to the reduction in the local symmetry (Fig. 4A).

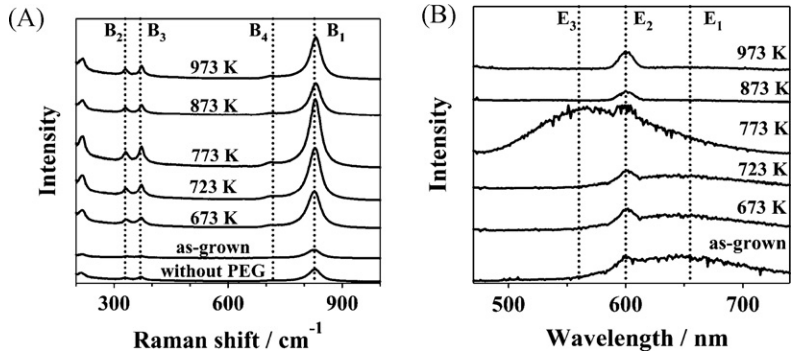

Fig. 4. (A) Raman spectra for $BiVO_4$ NRs with varying T_c the samples with varying T_c. (B) PL spectra for the $BiVO_4$ NRs with varying T_c.

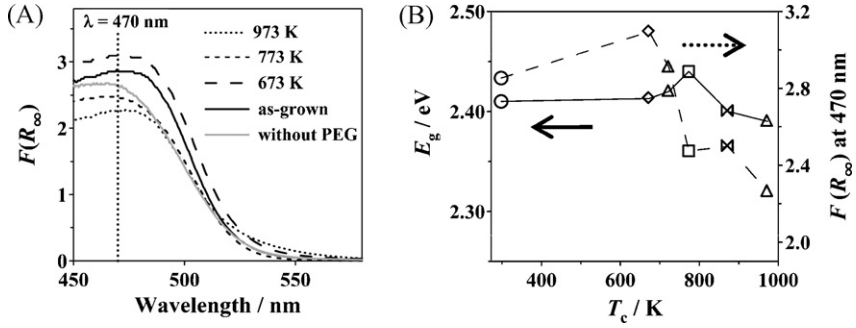

Fig. 5. (A) UV–vis absorption spectra for the samples with varying T_c: $F(R_\infty)$ expresses the Kubelka–Munk function. In each spectrum, the absorption edge due to the interband transition is located around 550 nm. (B) Plots of the band gap (E_g) and $F(R_\infty)$ at 470 nm as a function of T_c.

To gain information about the action of PEG, the absorption spectra of the reaction solutions were measured. Fig. 6 shows the absorption spectral change of the PEG solutions with the addition of NH_4VO_3. Neither PEG nor NH_4VO_3 has absorption at $\lambda > 500$ nm. As a result of the PEG addition, a new absorption band appears centered at 750 nm, intensifying with an increase in the NH_4VO_3 concentration. This finding recalls to us the take up of various metal cations in the helix of polyethylene oxide, and the application to solid polymer electrolyte [31]. A similar V^V species-PEG complex formation was postulated in a hydrothermal synthesis of single-crystal $VO_x{\cdot}nH_2O$ nanoribbons [32], although no direct evidence was provided. Refluxing of an ethanol solution of NH_4VO_3 produced VO^{2+} ions by the reduction with ethanol [33]. As shown in Fig. 6, the resulting VO^{2+} ions have an absorption around 785 nm, while it is different from that of $VO_2{}^-$ ions. Since the as-grown particle was identified as *ms*-$BiVO_4$, the absorption at 750 nm would be attributed to a VO_3-PEG complex rather than VO^{2+} ions. Note that the absorption appears when NH_4VO_3 and PEG are mixed at room temperature. Also, diffuse reflectance Fourier transform infrared (DRIFT) spectra were measured to examine the surface states of the *ms*-$BiVO_4$ NRs before and after heating. Fig. 7 shows DRIFT spectra of the as-grown *ms*-$BiVO_4$ NRs (a) and the sample heated at 673 K (b). In spectrum (a), the strong signal near 1300 cm^{-1} can be assigned to the stretching vibration of PEG, which disappear after heating at 673 K in spectrum (b). These results are indicative of the strong interactions between PEG and $VO_3{}^-$ in the starting solution, and between PEG and the $BiVO_4$ surface during the particle growth.

From these results, the reaction mechanism on the formation of *ms*-$BiVO_4$ NRs is inferred as follows: A complex is formed between $VO_3{}^-$ and PEG (S1), and $VO_3{}^-$ ions are stabilized. On addition of NaOH aqueous solution, BiO^+ ion is formed at pH > 4.5 (S2) [26]. BiO^+ ion reacts with $VO_3{}^-$ ion in a reaction field surrounded by PEG to yield $BiVO_4$ nuclei as formally expressed by Eq. (S3). In this

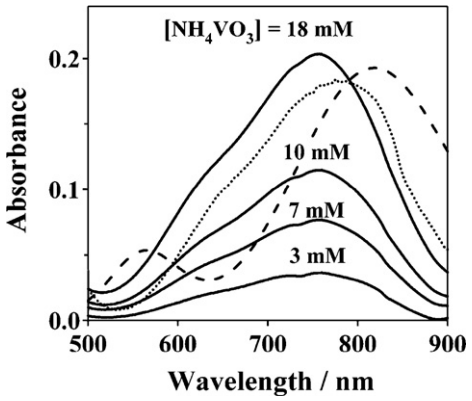

Fig. 6. The absorption spectral change of the PEG solutions with the addition of NH_4VO_3 (solid line). For comparison, the spectra of solutions of VO^{2+} ions (dotted line) and $VO_2{}^-$ ions (broken line) are shown.

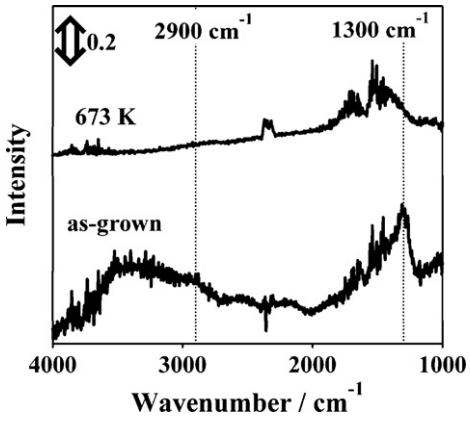

Fig. 7. DRIFT spectra of *ms*-$BiVO_4$ NRs before (a) and after (b) heating at 673 K.

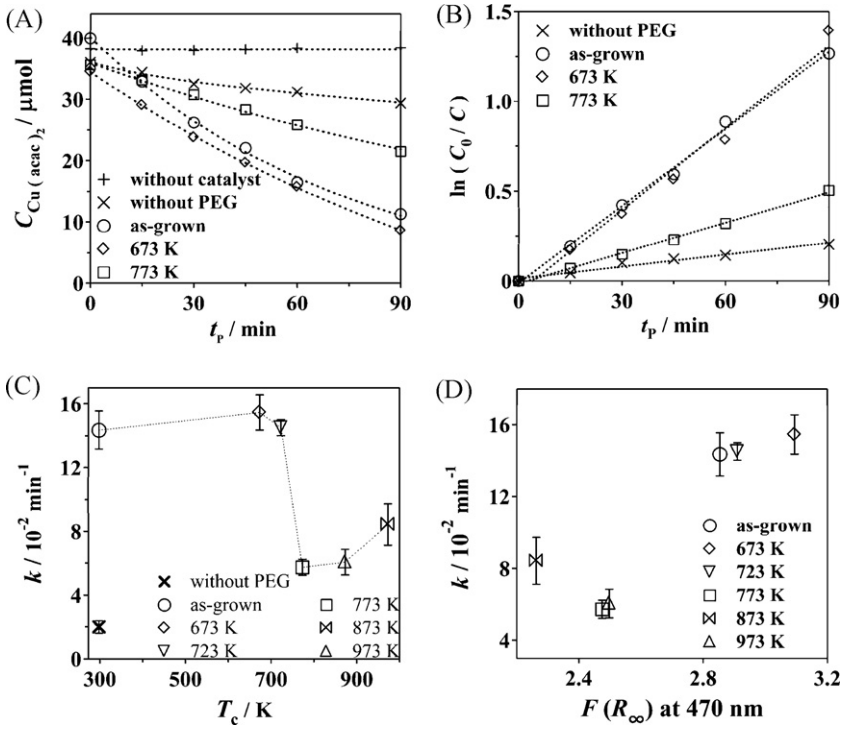

Fig. 8. (A) Time courses for the $Cu(acac)_2$ degradation under illumination of visible light ($\lambda > 430$ nm). Black solid circle shows the data for *ms*-$BiVO_4$ MCs prepared without PEG. (B) Plots of $\ln(C_0/C)$ vs. t_p. (C) Plots of the pseudo-first order rate constant (k, min^{-1}) vs. T_c. (D) Plots of k (min^{-1}) vs. $F(R_\infty)$ at 470 nm.

case, PEG provides a spacially restricted reaction filed for the BiO^+ and VO_3^- ions. Subsequently, particle growth of *ms*-$BiVO_4$ slowly occurs (S4) [22]. Macroscopically, the high viscosity of PEG would also prevent the large particle formation. Further, the formation of NRs may be explained by the weaker adsorption of PEG on the (1 1 2) crystal plane as compared to other crystal planes. In this manner, PEG controls the reactivity of the precursor, further acting as a soft template. These cooperative effects give rise to the formation of the *ms*-$BiVO_4$ NRs in this NAC-PEG route.

$$m\text{C—C—O} + VO_3^- \leftrightarrow (\text{C—C—O})_m\cdots VO_3^- \quad \text{(S1)}$$

$$Bi^{3+} + 2OH^- \rightarrow BiO^+ + H_2O \quad \text{(S2)}$$

$$BiO^+ + (\text{C—C—O})_m\cdots VO_3^- \rightarrow (\text{C—C—O})_m\cdots BiVO_4 \quad \text{(S3)}$$

$$(\text{C—C—O})_m\cdots n BiVO_4 \rightarrow (\text{C—C—O})_m\text{-adsorbed } BiVO_4 \text{ NR} \quad \text{(S4)}$$

To study the visible-light-activity of *ms*-$BiVO_4$ NRs, the *ms*-$BiVO_4$-photocatalytzed $Cu(acac)_2$ degradation was carried out as a test reaction. The detailed reaction mechanism has been reported in our preceding paper [9]. Fig. 8A shows time courses for the $Cu(acac)_2$ degradation under illumination of visible light ($\lambda > 430$ nm), where t_p denotes irradiation time. For comparison, the data on the *ms*-$BiVO_4$ MCs prepared without PEG is also shown (black solid circle). Both the irradiation and *ms*-$BiVO_4$ were necessary for the degradation to occur. The as-grown *ms*-$BiVO_4$ NR exhibits much higher activity as compared with *ms*-$BiVO_4$ MCs mainly because of the ca. 40-fold surface area (Table 1). In the *ms*-$BiVO_4$ NR system, irradiation leads to the $Cu(acac)_2$ degradation, for which rate significantly depends on T_c. As shown by Fig. 8B, this reaction apparently follows the first-order rate law. Fig. 8C shows plots of the pseudo-first order rate constant (k, min^{-1}) vs. T_c, and the numerical values are also shown in Table 1. Noticeably, the as-grown sample exhibits a high level of activity, which is somewhat increased by the postheating at $T_c = 673$ K in spite of the significant decrease in the surface area. This can be accounted for in terms of the increase in crystallinity enhancing the charge separation [25]. At $T_c = 773$ K, the k abruptly decreases nevertheless of the increase in crystallinity. At $T_c \geq 773$ K, the k hardly changes, for which the decrease in the surface area is mainly responsible. Very recently, Wang et al. have reported a similar method using PEG-4000 for the preparation of *ms*-$BiVO_4$ nano-leaves ($S_{BET} = 9.2\ m^2\ g^{-1}$), which shows a visible-light-activity for O_2 generation from an aqueous $AgNO_3$ solution exceeding that of *ms*-$BiVO_4$ prepared by the solid-state reaction [34]. In contrast to the present system, the activity remarkably increases by the postheating at 673 K. These results point to the importance of the compatibility of large surface area and high crystallinity for the photocatalytic activity of $BiVO_4$, while the former is more significant than the latter. The small effective masses of electrons ($\sim 0.9m_0$) and holes ($\sim 0.7m_0$) [29] should guarantee their large mobility in $BiVO_4$. In the NRs, the small transit time for the diffusion of the charge carriers to the surface reaction sites may compensate the low crystallinity to some degree.

However, the remarkably low photocatalytic activity of *ms*-$BiVO_4$ with $T_c = 773$ K cannot be explained in terms of the idea drawn from the TiO_2 photocatalysis [21]. The relation between k (min^{-1}) vs. $F(R_\infty)$ at 470 nm is shown in Fig. 8D. Importantly, there is a positive correlation between k and $F(R_\infty)$ at 470 nm. This finding indicates that the local high symmetry of the VO_4 tetrahedron increasing the absorption intensity for the direct band gap excitation (Fig. 4A) is a governing factor for its photocatalytic activity. Consequently, the high local symmetry of VO_4 tetrahedron in addition to the large surface area and high crystallinity is of great importance to achieve the high visible-light-activity of *ms*-$BiVO_4$.

From a viewpoint of environmental catalysis, the recovery of Cu^{2+} ions is important concomitantly with the decomposition of acac-species in the photocatalytic reaction of $Cu(acac)_2$. In deaerated solution systems, visible-light-induced deposition of Cu on the $BiVO_4$ took place, whereas no Cu was deposited from aerated solutions [9]. Fig. 9 compares the recovery of Cu^{2+} ions from the deaerated $Cu(acac)_2$ solution (initial pH 8.7) for the $BiVO_4$ prepared with and without PEG ($T_c = 673$ K). In each system, the amount of Cu photodeposited increases with increasing t_p, reaching constant

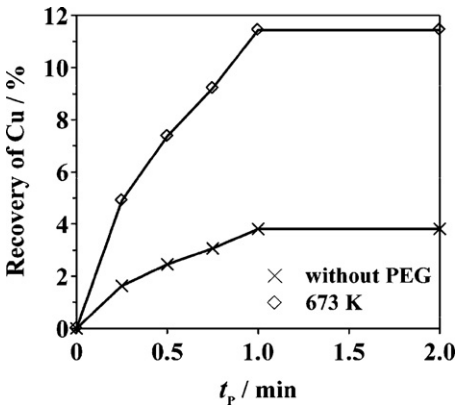

Fig. 9. Recovery of Cu^{2+} ions from deaerated $Cu(acac)_2$ solution (initial pH 8.7) for the samples prepared with and without PEG as a function of irradiation time (t_p).

at $t_p > 1$ h. The saturated value for the *ms*-$BiVO_4$ NRs is approximately three times greater than that for *ms*-$BiVO_4$ MCs, which could also be explained mainly by the larger surface area of *ms*-$BiVO_4$ NRs. Note that the recovery can be increased up to ~90% by adjusting the pH solution at 10.4 as reported in our preceding paper [9].

4. Conclusions

Monoclinic sheelite $BiVO_4$ NRs have been prepared by a NAC-PEG method using PEG as a soft template. The as-grown *ms*-$BiVO_4$ NRs exhibits a much higher activity for the degradation of $Cu(acac)_2$ under illumination of visible-light as compared to *ms*-$BiVO_4$ MCs. This study has shown that the high local symmetry of VO_4 tetrahedron as well as the large surface area and high crystallinity is a crucial factor for the visible-light-activity of *ms*-$BiVO_4$. The present "green" synthetic route should be widely applied for preparing various functional metal oxide nanoparticles.

Acknowledgements

This work was supported by a Grant-in-Aid for Scientific Research (B) No. 20350097 from the Ministry of Education, Science, Sport, and Culture, Japan, by the Nippon Sheet Glass Foundation for Materials Science and Engineering, and by the Sumitomo Foundation.

References

[1] M.R. Hoffmann, S.T. Martin, W. Choi, D.W. Bahnemann, Chemical Reviews 95 (1995) 69.
[2] G. Liu, L. Wang, H.G. Yang, H.-M. Cheng, G.Q. Lu, Journal of Materials Chemistry 20 (2010) 831.
[3] H. Tada, Q. Jin, H. Nishijima, H. Yamamoto, M. Fujishima, S.-i. Okuoka, T. Hattori, Y. Sumida, H. Kobayashi, Angewandte Chemie International Edition 50 (2011) 3501.
[4] A. Kudo, Y. Miseki, Chemical Society Reviews 38 (2009) 253.
[5] A. Kudo, K. Ueda, H. Kato, I. Mikami, Catalysis Letters 53 (1998) 229.
[6] D. Ke, T. Peng, L. Ma, P. Cai, P. Jiang, Applied Catalysis A-General 350 (2008) 111.
[7] S. Kohtani, S. Makino, A. Kudo, K. Tokumura, Y. Ishigaki, T. Matsunaga, O. Nikaido, K. Hayakawa, R. Nakagaki, Chemistry Letters (2002) 660.
[8] L. Zhang, D. Chen, X. Jiao, Journal of Physical Chemistry B 110 (2006) 2668.
[9] S.-i. Naya, M. Tanaka, H. Tada, Langmuir 27 (2011) 10334.
[10] N.C. Castillo, A. Heel, T. Graule, C. Pulgarin, Applied Catalysis B: Environmental 95 (2010) 335.
[11] N.C. Castillo, L. Ding, A. Heel, T. Graule, C. Pulgarin, Journal of Photochemistry and Photobiology A: Chemistry 216 (2010) 221.
[12] B. Xie, H. Zhang, P. Cai, R. Qiu, Y. Xiong, Chemosphere 63 (2006) 956.
[13] M. Gotic, S. Music, M. Ivanda, M. Soufek, S. Popovic, Journal of Molecular Structure 744–747 (2005) 535.
[14] S.S. Dunkle, R.J. Helmich, K.S. Suslick, Journal of Physical Chemistry C 13 (2009) 11980.
[15] Z. Zhang, W. Wang, M. Shang, W. Yin, Catalysis Communications 11 (2010) 982.
[16] A.M. de la Cruz, U.M. Garcia Perez, Materials Research Bulletin 45 (2010) 135.
[17] G. Xi, J. Ye, Chemical Communications 46 (2010) 1893.
[18] Y. Zhou, K. Vuille, A. Heel, B. Probst, R. Kontic, G.R. Patzke, Applied Catalysis A 375 (2010) 140.
[19] X. Meng, L. Zhang, H. Dai, Z. Zhao, R. Zhang, Y. Liu, Materials Chemistry and Physics 125 (2011) 59.
[20] A. Kudo, K. Omori, H. Kato, Journal of the American Chemical Society 121 (1999) 11459.
[21] S. Ito, S. Inoue, H. Kawada, M. Hara, M. Iwasaki, H. Tada, Journal of Colloid and Interface Science 216 (1999) 59.
[22] Y.-i. Inubushi, R. Tamaki, M. Iwasaki, H. Tada, S. Ito, Journal of Colloid and Interface Science 200 (1998) 220.
[23] M. Iwasaki, M. Hara, H. Kawada, H. Tada, S. Ito, Journal of Colloid and Interface Science 224 (2000) 202.
[24] Q. Jia, A. Kudo, in: M. Iwamoto (Editor-in-Chief), How to Prepare Heterogeneous and Homogeneous Catalysts, NTS, Tokyo, 2011, p. 523.
[25] H. Tada, M. Tanaka, Langmuir 13 (1997) 360.
[26] J. Yu, A. Kudo, Advanced Functional Materials 16 (2006) 2163.
[27] A. Zhang, J. Zhang, Materials Letters 63 (2009) 1939.
[28] Q. Jin, M. Fujishima, H. Tada, Journal of Physical Chemistry C 115 (2011) 6478.
[29] Z. Zhao, Z. Li, Z. Zou, Physical Chemistry Chemical Physics 13 (2011) 4746.
[30] N. Serpone, D. Lawless, R. Khairutdinov, Journal of Physical Chemistry 99 (1995) 16646.
[31] M.B. Armand, J.M. Chabango, M. Duclot, in: P. Vashsta, J.N. Mundy, G.K. Shenoy (Eds.), Fast Ion Transport in Solids, Elsevier/North-Holland, New York, 1979, p. p131.
[32] L. Kong, Z. Liu, M. Shao, Q. Xie, W. Yu, Y. Qian, Journal of Solid State Chemistry 177 (2004) 690.
[33] F.A. Cotton, G. Wilkinson, Advanced Inorganic Chemistry, 2nd ed., John Wiley & Sons, New York, 1972.
[34] Z. Wang, W. Luo, S. Yan, J. Feng, Z. Zhao, Y. Zhu, Z. Li, Z. Zou, CrystEngComm 13 (2011) 2500.